

Data-driven approach for modelling Reynolds stress tensor with invariance preservation

Xuepeng Fu,^{1,2} Shixiao Fu,^{1,2,*} Chang Liu,³ and Mengmeng Zhang^{1,2}

¹*State Key Laboratory of Ocean Engineering, Shanghai Jiao Tong University, Shanghai, 200240, China*

²*Institute of Polar and Ocean Technology, Institute of Marine Equipment,
Shanghai Jiao Tong University, Shanghai, 200240, China*

³*Department of Physics, University of California, Berkeley, CA, 94720, USA*

(Dated: March 31, 2023)

The present study represents a data-driven turbulent model based machine learning algorithm with Galilean invariance preservation. The fully connected neural network (FCNN) and tensor basis neural network (TBNN) [Ling et al. (2016)] are established. The models are trained based on five kinds of flow cases with Reynolds Averaged Navier-Stokes (RANS) and high-fidelity data. The mappings between two invariant sets and the Reynolds stress anisotropy tensor are trained. The prediction of the Reynolds stress anisotropy tensor is treated as user's defined RANS turbulent model with a modified turbulent kinetic energy transport equation. The results show that the FCNN and TBNN models can accurately predict the anisotropy tensor and turbulent state compared with the traditional RANS model for square duct flow and periodic flow cases. The machine learning based turbulent model with turbulent kinetic energy consideration can improve the prediction precision compared with only mean strain rate tensor and mean rotation rate tensor based models. The TBNN model is able to predict a better flow velocity profile due to a prior physical knowledge.

I. INTRODUCTION

In most industrial applications where resources and time are limited, the choice is often made to solve the Reynolds averaged Navier-Stokes equations (RANS) in turbulent flow simulations [1]. The RANS model employed time-averaging method to eliminate temporal dependency for stationary turbulence, which will produce a term named Reynolds stress need turbulence modelling closure. Turbulence modeling is a primary source of uncertainty in the computational fluid dynamics (CFD) simulations of turbulent flows. Many nonlinear eddy models based on the Boussinesq approximation, such as the $k - \epsilon$ and $k - \omega$ models and Reynolds stress transport models (RSTM), have been proposed to model Reynolds stress [2]. However, RANS predictions may be highly inaccurate for some canonical flows due to the poor description of the effects of the Reynolds stresses on the mean flow based on Boussinesq approximation based turbulence model [3]. On the other hand, some CFD data with high fidelity, such as direct numerical simulation (DNS) and highly resolved large eddy simulation (LES), have been reported due to the use of high-performance computers and big data techniques. Research on data-driven turbulent models has been carried out in the last few years to improve the accuracy of turbulence model, in which supervised machine learning (ML) algorithms have been applied mostly in this research field [4].

* shixiao.fu@sjtu.edu.cn

The pioneer research of ML algorithms in fluid mechanic was to develop a partial differential equation (PDE) solution method by directly mapping the properties of the flow field to the velocity field. Milano and Koumoutsakos [5] trained a neural network based on velocity fields of DNS data to reconstruct the near wall turbulent flow. Raissi *et al.* [6] develop the physics-informed neural networks (PINN) with modified loss function incorporates PDE residuals. More specifically, several proposed investigations already exist based on different algorithms for establishing an improved Reynolds stress prediction model [7]. Tracey *et al.* [8] established a Reynolds stress anisotropy prediction model by kernel-based regression algorithms. Duraisamy *et al.* [9] applied two types of ML methods, neural networks and Gaussian processes, to model intermittency in transitional turbulence. Zhang and Duraisamy [10] used a multiscale Gaussian process to model turbulence production in channel flow. Ling and Templeton [11] used random forests to predict regions of high model form uncertainty in RANS results. [12] established a turbulent model based on the ensemble Kalman filter method. In the latter case, uncertainty quantification has been applied to develop predictive models in the absence of data by incorporating stochastic terms that are intended to capture the effect of modeling assumptions [13–15]. Reynolds stress is treated as an ellipsoid structure with perturbation and rigid-body rotation in the studies mentioned above . The Euler-angle-based representations of the perturbation is considered for rotation. The predictions in different coordinate systems needs to be transformed.

Galilean invariance, which states that laws do not alter in different inertial frames of reference, is a fluid mechanics property pertaining to the law of motion. Specifically, no matter how the frame of reference is rotated, reflected, or translated, the pressure and velocity magnitude will remain unchanged. As mentioned above, the Reynolds stress is described as a three-dimensional ellipsoid with Euler-angle-based representations to ensure Galilean invariance [16]. Another approach to meet Galilean invariance in turbulent modelling is establishing the mapping based on invariance obtained from flow field data. Ling *et al.* [17] investigated a machine learning-based turbulent prediction model. The inputs were invariant terms derived from the flow fields. Duraisamy *et al.* [9] and Ling and Templeton [11] applied feature selection algorithms to optimize the input features. These models established the mapping between invariants and Quantities of Interest (QoIs, e.g. second principal invariant of Reynolds stress anisotropy tensor [17]). No representation constraint based on a prior knowledge is applied for modelling. Pope [18] proposed a complete representation of Reynolds stress anisotropy tensor with invariants set derived from turbulence data based on tensor valued function representation theory [19]. Ling *et al.* [20] established the neural network to meet the turbulent model proposed by Pope [18] named tensor based neural network (TBNN). The TBNN embeds tensor functions into the machine learning algorithm for turbulence simulation. In Pope's turbulent model, only mean strain rate tensor and mean rotation rate tensor are taken into consideration which may lead to inaccuracy.

In the present study, the complete invariants sets based on mean strain rate tensor, mean rotation rate tensor and turbulent kinetic energy gradient are included for turbulence modelling based on a fully connected neural network and a tensor basis neural network algorithm. Five different types of flow cases are involved for training process. Two different types of input data of square duct flow and periodic flow are applied for analyzed. This paper is structured as follows. Section II introduces the methodology of invariant-based turbulent models and the framework of the present study. Section III discusses the predictions of the Reynolds stress anisotropy tensor and flow velocity profile of square duct flow and periodic flow. Section IV offers conclusions and future research directions. The results demonstrate considering the turbulent energy gradient can increase turbulence prediction accuracy, but this leads to an excess of independent variables. Hence, feature selection researches [9] will be carried out for future work.

II. METHOD

A. Reynolds-averaged Navier-Stokes equation

For an incompressible, constant density and zero gravity flow, the following RANS equations apply:

$$\frac{\partial \bar{u}_i}{\partial x_i} = 0, \quad (1)$$

$$\frac{\partial \bar{u}_i}{\partial t} + \bar{u}_j \frac{\partial \bar{u}_i}{\partial x_j} = -\frac{1}{\rho} \frac{\partial \bar{p}}{\partial x_i} + \frac{\partial}{\partial x_j} \left(\nu \frac{\partial \bar{u}_i}{\partial x_j} - \overline{u'_i u'_j} \right), \quad (2)$$

where \bar{u}_i is the mean velocity, \bar{p} is the mean pressure and ν is the kinematic viscosity. The Reynolds stress term $\overline{u'_i u'_j}$ (also $\boldsymbol{\tau}$) can be expressed as:

$$\tau_{ij} = \overline{u'_i u'_j} = \frac{2}{3} k \delta_{ij} + a_{ij}, \quad (3)$$

where $k = \frac{1}{2} \text{tr}(\overline{u'_i u'_j})$ is the turbulence kinetic energy, δ_{ij} is the Kronecker delta and a_{ij} is the Reynolds stress anisotropy tensor. The anisotropic part of the Reynolds stresses is important and effective in transporting momentum. The isotropic part is simply absorbed into a modified pressure term.

Based on the Boussinesq approximation ($a_{ij} = -2\nu_t S_{ij}$), the RANS equations can be written as:

$$\frac{\partial \bar{u}_i}{\partial x_i} = 0, \quad (4)$$

$$\frac{\partial \bar{u}_i}{\partial t} + \bar{u}_j \frac{\partial \bar{u}_i}{\partial x_j} = -\frac{1}{\rho} \frac{\partial \bar{p}'}{\partial x_i} + 2(\nu + \nu_t) \frac{\partial S_{ij}}{\partial x_j}, \quad (5)$$

where $\bar{p}' = \bar{p} + \frac{2}{3} \rho k$, ν_t is the turbulent viscosity and S_{ij} is the mean strain rate tensor. The turbulent viscosity ν_t is modeled by PDEs in different turbulent models. For example, the $k - \omega$ turbulent model is modeled by solving the governing equations of k and ω and $\nu_t = k/\omega$:

$$\tau_{ij} = \frac{k}{\omega} S_{ij}, \quad \omega = \frac{\varepsilon}{C_\mu k}, \quad (6)$$

where ω is the specific turbulence dissipation rate, and ε is the turbulence dissipation. $C_\mu = 0.09$ is applied in the present study [21].

Another class of RANS turbulence models that will briefly be discussed is the Reynolds stress transport model (RSTM). Therein, the Reynolds stress is modeled by the governing equation of Reynolds stress $\overline{u'_i u'_j}$ [22]. RSTM turbulence models are more likely to diverge than Boussinesq approximation based models. Consequently, the Boussinesq approximation based models remain the preferred method for many flow cases.

B. Reynolds stress and realizability

As a positive semi-definite matrix, the eigenvalues of Reynolds stress τ_{ij} are real and non-negative:

$$\tau_{ii} \geq 0, \quad i = 1, 2, 3, \quad (7)$$

Considering Cauchy-Schwarz inequality:

$$\tau_{ij}^2 \leq \tau_{ii} \tau_{jj}, \quad i, j = 1, 2, 3 \quad (i \neq j). \quad (8)$$

Therefore, the diagonal values of the Reynolds stress are within $[0, 2k]$ based on Eq. (3), and the off-diagonal values are within $[-k, k]$. The Reynolds stress tensor can be expressed as:

$$\tau_{ij} = 2k \left(\frac{1}{3} \delta_{ij} + b_{ij} \right), \quad (9)$$

where b_{ij} (also \mathbf{b}) is the non-dimensional Reynolds stress anisotropy tensor, which can be expressed as:

$$b_{ij} = \frac{\tau_{ij}}{2k} - \frac{1}{3} \delta_{ij}. \quad (10)$$

Considering Eq. (8), the diagonal and off-diagonal values of non-dimensional Reynolds stress anisotropy tensor meet:

$$b_{ij} \leq b_{ii} + b_{jj} + \frac{2}{3}, \quad i, j = 1, 2, 3 \quad (i \neq j). \quad (11)$$

Then, the Reynolds stress tensor can be transformed as follows by eigenvalue decomposition:

$$\tau_{ij} = 2k \left(\frac{1}{3} \delta_{ij} + v_{in} \Lambda_{nl} v_{jl} \right), \quad (12)$$

where v_{ij} is the eigenvector and $\Lambda_{ij} = \text{diag}[\lambda_1, \lambda_2, \lambda_3]$ is the diagonal matrix containing the eigenvalues λ_i of b_{ij} with $\lambda_1 + \lambda_2 + \lambda_3 = 0$ of b_{ij} .

The eigenvalues of the Reynolds stress tensor (ϕ_i) can be related to the eigenvalues of the Reynolds stress anisotropy tensor (λ_i) by:

$$\lambda_i = \frac{\phi_i}{2k} - \frac{1}{3}. \quad (13)$$

The ϕ_i falls in $[0, 2k]$, then λ_i are in the range $[-\frac{1}{3}, \frac{2}{3}]$. The different eigenvalues satisfy the physical boundaries as [23]:

$$\begin{aligned} \lambda_1 &\geq (3|\lambda_2| - \lambda_2) / 2 & (\lambda_1 \geq \lambda_2 \geq \lambda_3) \\ \lambda_1 &\leq 1/3 - \lambda_2 \end{aligned} \quad (14)$$

Overall, there are the following fundamental constraints of the realizability of the non-dimensional Reynolds stress anisotropy tensor b_{ij} : (1) the diagonal value of b_{ij} should be greater than $-\frac{1}{3}$, and the trace should be 0. (2) The value of b_{ij} should satisfy Eq. (11). (3) The eigenvalues of b_{ij} should meet Eq. (14).

There exist three principle invariants of b_{ij} : $I_1 = b_{ii}$, $I_2 = b_{ij}b_{ji}$, and $I_3 = b_{ij}b_{in}b_{jn}$. I_1 is the trace of b_{ij} equal to zero. Therefore, there exist only two independent invariants of the anisotropy tensor I_2 and I_3 . Many realizable states of turbulence anisotropy (noted as anisotropy-invariant maps) have been proposed, such as the Lumley triangle [24] and Barycentric map [23]. Fig. 1 displayed turbulent states of periodic hills at $Re = 10545$ [25] with a Lumley triangle [26]. Fig. 2 displays the Barycentric map [23] of the same flow case. Different from Lumley triangle, an equilateral triangle is used for plotting the physical realizability in the Barycentric map as Fig. 2(a) shows. We can color the Barycentric map with Red-Green-Blue(RGB) map as colormap shown in Fig. 2(b), and the flow field can be colored for visualization based colormap of Fig. 2(b) as Fig. 2(c) shows. In the present study, the turbulent state is refereed to the anisotropy in the flow field. There exist three corners of Barycentric map refer to three limiting state of turbulence: one-component state (1C), two-component state (2C) and three-component state (3C). The 1C state means turbulence exists only one component of turbulent kinetic energy, turbulence in an area of this type is only along one direction. The 2C state of turbulence means one component of turbulent kinetic energy vanishes with the remaining two being equal, and 3C state refer to isotropic turbulence.

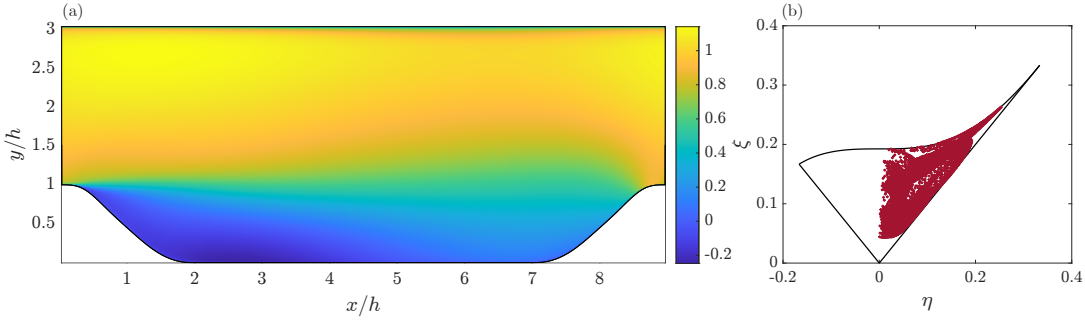


FIG. 1: Periodic hills at $Re = 10545$ [25]. (a) mean velocity U ; (b) anisotropy-invariant map of the Lumley triangle.

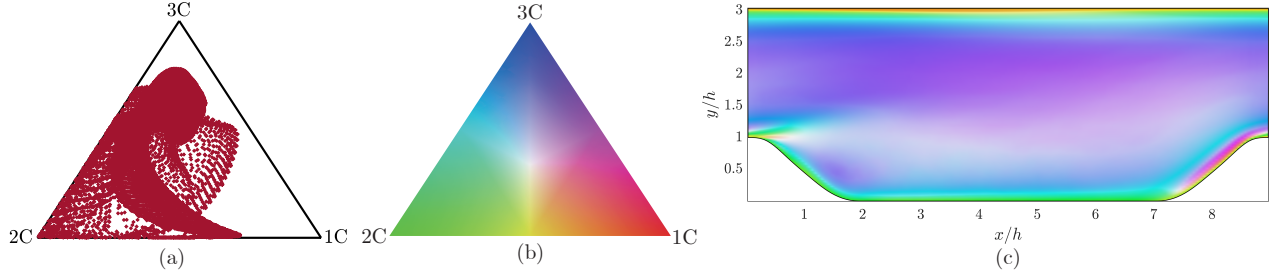


FIG. 2: Turbulent states of periodic hills at $Re = 10545$ [25] with Barycentric map. (a) Barycentric map; (b) colored Barycentric map used for colorbar; (c) anisotropy in the flow field (turbulent state).

C. Representation of isotropic tensor-valued function

The Navier-Stokes equations are Galilean invariant, which means that the equations are the same in all inertial frames of reference, and the model of the Reynolds stress anisotropy tensor should follow this constraint. Otherwise, the predicted results will be different for flow fields with axes defined in different directions.

Define a scalar-valued function $f : \{\mathbb{R}^{3 \times 3}, \mathbb{R}^{1 \times 3}\} \rightarrow \mathbb{R}$. The necessary and sufficient condition that f is Galilean invariant applied when:

$$f(\mathbf{Q}\mathbf{A}_1\mathbf{Q}^T, \mathbf{Q}\mathbf{A}_2\mathbf{Q}^T, \dots, \mathbf{Q}\mathbf{A}_n\mathbf{Q}^T, \mathbf{Q}\mathbf{v}) = f(\mathbf{A}_1, \mathbf{A}_2, \dots, \mathbf{A}_n, \mathbf{v}), \quad \mathbf{A}_i \in \mathbb{R}^{3 \times 3}, \quad \mathbf{v} \in \mathbb{R}^{1 \times 3}, \quad \mathbf{Q} \in O(3), \quad (15)$$

where $O(3)$ is the orthogonal group, and the function f is called as isotropic function. Furthermore, an isotropic tensor-valued function $\mathbf{G} : \mathbb{R}^{3 \times 3} \rightarrow \mathbb{R}^{3 \times 3}$ with one variable \mathbf{A} can be spectrally decomposed as:

$$\mathbf{G}(\mathbf{A}) = \sum_{i=1}^n t_i(\lambda_1, \lambda_2, \lambda_3) \mathbf{E}_i, \quad (16)$$

where $t_i : \mathbb{R}^3 \rightarrow \mathbb{R}$ is a scalar function of eigenvalues of \mathbf{A} , λ_i are the invariants of \mathbf{A} , and \mathbf{E}_i is the tensor basis.

As per the Cayley-Hamilton theorem [27], there exists a limited number of linearly independent tensors bases (form-invariants) that can be formed from \mathbf{A} . It can be derived from the polynomial expression of \mathbf{A} with three tensor bases as \mathbf{I} (identity tensor), \mathbf{A} and \mathbf{A}^2 . Then Eq. (16) can be further expressed as:

$$\mathbf{G}(\mathbf{A}) = \sum_{i=1}^3 t_i(\lambda_1, \lambda_2, \lambda_3) \mathbf{G}_i, \quad \mathbf{G}_i = \mathbf{A}^{i-1}. \quad (17)$$

In the present study, the normalized mean strain rate tensor and mean rotation rate tensor are defined as:

$$\begin{aligned}\mathbf{S} = \hat{\mathbf{S}}_{ij} &= \frac{S_{ij}}{(|\alpha| + |S_{ij}|)}, \quad S_{ij} = \frac{1}{2} \left(\frac{\partial \bar{u}_i}{\partial x_j} + \frac{\partial \bar{u}_j}{\partial x_i} \right), \\ \mathbf{R} = \hat{\mathbf{R}}_{ij} &= \frac{R_{ij}}{(|\alpha| + |R_{ij}|)}, \quad R_{ij} = \frac{1}{2} \left(\frac{\partial \bar{u}_i}{\partial x_j} - \frac{\partial \bar{u}_j}{\partial x_i} \right),\end{aligned}\quad (18)$$

where $\alpha = \varepsilon/k$ is the normalization factor. The normalized mean strain rate tensor is expressed as S_{ij}/α in the previous research [18, 20]. The normalization method in the present study will allow a smaller range of values.

The traditional turbulent model based on the Boussinesq approximation assumes that the Reynolds stress anisotropy tensor is related to the mean strain rate tensor $\mathbf{b} \sim \mathbf{S}$. If the mean rotation rate tensor is added to the independent variable, a tensor-valued function $\mathbf{b} = \mathbf{F}(\mathbf{S}, \mathbf{R})$ is adequately modeled.

Wang and Smith have investigated the representation theorem for isotropic functions [28, 29]. Eringen and Zheng summarized complete and irreducible invariants and tensors basis of second-order symmetric tensors, asymmetric tensors and vectors [30, 31]. For the second-order symmetric tensor A and asymmetric tensor R , the complete and irreducible set contains 7 invariants and 10 tensor bases. The invariants can be expressed as:

$$\tilde{\lambda}_1 = \text{tr}(\mathbf{S}), \quad \tilde{\lambda}_2 = \text{tr}(\mathbf{S}^2), \quad \tilde{\lambda}_3 = \text{tr}(\mathbf{S}^3), \quad \tilde{\lambda}_4 = \text{tr}(\mathbf{R}^2), \quad \tilde{\lambda}_5 = \text{tr}(\mathbf{SR}^2), \quad \tilde{\lambda}_6 = \text{tr}(\mathbf{S}^2\mathbf{R}^2), \quad \tilde{\lambda}_7 = \text{tr}(\mathbf{S}^2\mathbf{R}^2\mathbf{SR}) \quad (19)$$

In the 7 invariants, $\tilde{\lambda}_1 = 0$ due to the continuity equation of incompressible fluids, and $\tilde{\lambda}_7^2$ has an implicit function connection with the previous six invariants $\tilde{\lambda}_7^2 = t(\tilde{\lambda}_1, \dots, \tilde{\lambda}_6)$, with the proof is displayed in Appendix A. Therefore, the minima set contains five independent invariants. The tensor-valued function $\mathbf{F} : \mathbb{R}^{3 \times 3} \rightarrow \mathbb{R}^{3 \times 3}$ can be expressed as:

$$\mathbf{b} = \sum_{i=1}^{10} g_i(\lambda_1, \dots, \lambda_5) \mathbf{T}^i, \quad (20)$$

where:

$$\begin{cases} \mathbf{T}^1 = \mathbf{S}, & \mathbf{T}^6 = \mathbf{R}^2\mathbf{S} + \mathbf{S}\mathbf{R}^2 - \frac{2}{3}\mathbf{I} \cdot \text{tr}(\mathbf{SR}^2), \\ \mathbf{T}^2 = \mathbf{S}\mathbf{R} - \mathbf{R}\mathbf{S}, & \mathbf{T}^7 = \mathbf{R}\mathbf{R}^2 - \mathbf{R}^2\mathbf{S}\mathbf{R}, \\ \mathbf{T}^3 = \mathbf{S}^2 - \frac{1}{3}\mathbf{I} \cdot \text{tr}(\mathbf{S}^2), & \mathbf{T}^8 = \mathbf{S}\mathbf{R}\mathbf{S}^2 - \mathbf{S}^2\mathbf{R}\mathbf{S}, \\ \mathbf{T}^4 = \mathbf{R}^2 - \frac{1}{3}\mathbf{I} \cdot \text{tr}(\mathbf{R}^2), & \mathbf{T}^9 = \mathbf{R}^2\mathbf{S}^2 + \mathbf{S}^2\mathbf{R}^2 - \frac{2}{3}\mathbf{I} \cdot \text{tr}(\mathbf{S}^2\mathbf{R}^2), \\ \mathbf{T}^5 = \mathbf{R}\mathbf{S}^2 - \mathbf{S}^2\mathbf{R}, & \mathbf{T}^{10} = \mathbf{R}\mathbf{S}^2\mathbf{R}^2 - \mathbf{R}^2\mathbf{S}^2\mathbf{R}, \end{cases} \quad (21)$$

$$\lambda_1 = \text{tr}(\mathbf{S}^2), \quad \lambda_2 = \text{tr}(\mathbf{R}^2), \quad \lambda_3 = \text{tr}(\mathbf{S}^3), \quad \lambda_4 = \text{tr}(\mathbf{R}^2\mathbf{S}), \quad \lambda_5 = \text{tr}(\mathbf{R}^2\mathbf{S}^2). \quad (22)$$

This turbulent model was first proposed by Pope [18] and the same notation is applied in the present study.

D. Tensor basis neural network

Ling *et al.* [20] developed a neural network architecture named the tensor basis neural network (TBNN) to implement Pope's turbulent model. Fig. 3 represents the schematic of TBNN-5. The TBNN-5 means TBNN with five input features which is the same with Pope's turbulent model. A fully connected neural network with five input neurons

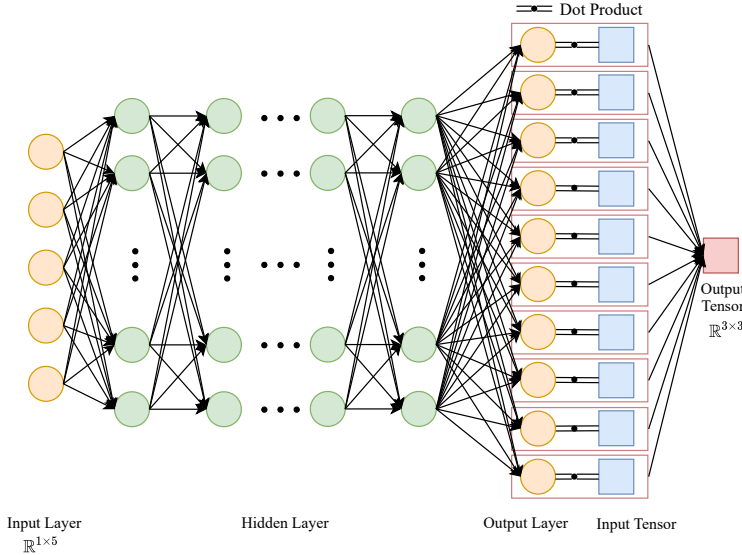


FIG. 3: Schematic of TBNN-5. A fully connected neural network contains an input layer (five invariants based on \mathbf{S} and \mathbf{R}), hidden layer and output layer (ten scalar function values in Eq. (20)). The output tensor is the sum of the dot product of the output layer values and ten input tensors (ten tensor bases based on \mathbf{S} and \mathbf{R}).

and ten output neurons produces $g_i (1 \leq i \leq 10)$. The output layer values then are applied as dot product with the 10 input tensors. The loss function is the mean square error (MSE) of the output tensor.

In the $k - \omega$ turbulent model, the Reynolds stress tensor is modeled by Eq. (6), which means that the Reynolds stress anisotropy tensor of the RANS model is also a deterministic function of \mathbf{S} . In the present study, the discrepancy of $\Delta\mathbf{b}$ between the high-fidelity data and RANS data will slightly deduce the scalar function g_i (see Appendix B). Therefore, a tensor-valued function $\mathbf{F}_1 : \mathbb{R}^{3 \times 3} \rightarrow \mathbb{R}^{3 \times 3}$ is trained by the neural network the same as the TBNN in the present study:

$$\Delta\mathbf{b} = \sum_{i=1}^{10} g_i(\lambda_1, \dots, \lambda_5) \mathbf{T}^i. \quad (23)$$

The neural network structure is the same as Fig. 3 shows, and the values of g_i and \mathbf{T}^i are the same as Eq. (21) and Eq. (22) display. Meanwhile, a fully connected neural network (FCNN) model is also trained to obtain regression function \mathbf{F} as Fig. 4 shows. The input layer contains the five invariants, and the output layer is the six independent values of $\Delta\mathbf{b}$.

The mean strain rate tensor and mean rotation rate tensor are considered in the Pope turbulent model [18]. In the present study, we account for the turbulent kinetic energy gradient in turbulent modeling, which includes establishing a tensor function as follows:

$$\Delta\mathbf{b} = \mathbf{F}_2(\mathbf{S}, \mathbf{R}, \widehat{\nabla k}), \quad (24)$$

where $\widehat{\nabla k}$ is the non-dimensional ∇k by non-dimensional coefficient $\frac{\sqrt{k}}{\epsilon}$:

$$\widehat{\nabla k} = \frac{\nabla k}{(|\frac{\sqrt{k}}{\epsilon}| + |\nabla k|)}. \quad (25)$$

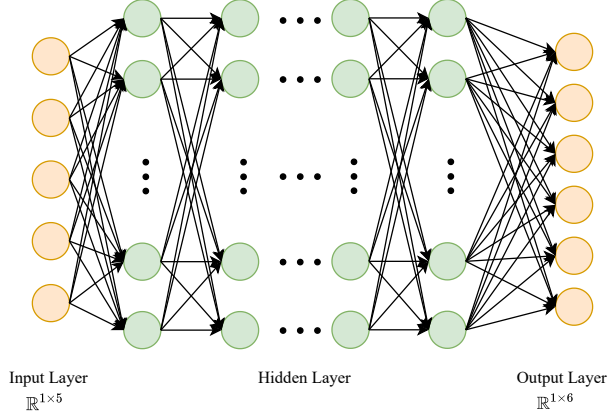


FIG. 4: Schematic of FCNN-5 model. A fully connected neural network contains an input layer (five invariants based on \mathbf{S} and \mathbf{R}), hidden layer and output layer (six independent values of $\Delta\mathbf{b}$).

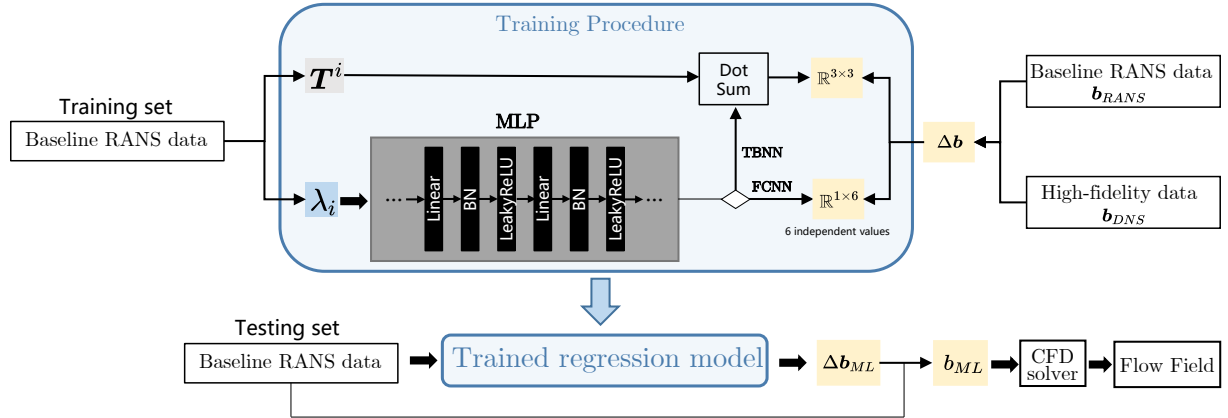


FIG. 5: Framework of the present study. \mathbf{T}^i and λ_i are the tensor basis and invariants obtained from the training set RANS flow case; the multilayer perceptron (MLP) with linear, batch normalization (BN) and LeakyReLU activator layers are established; the TBNN method applies a dot product with the MLP output layer ($\mathbb{R}^{1 \times 10}$) with corresponding \mathbf{T}^i and summary; the FCNN method will directly output $\Delta\mathbf{b}$.

The complete invariants set based on S , R and ∇k are as follows: [30, 31]:

$$\left\{ \begin{array}{ll} \mathbf{T}^1 = \mathbf{S}, & \mathbf{T}^6 = \mathbf{R}^2 \mathbf{S} + \mathbf{S} \mathbf{R}^2 - \frac{2}{3} \mathbf{I} \cdot \text{tr}(\mathbf{S} \mathbf{R}^2), \\ \mathbf{T}^2 = \mathbf{S} \mathbf{R} - \mathbf{R} \mathbf{S}, & \mathbf{T}^7 = \mathbf{R} \mathbf{R}^2 - \mathbf{R}^2 \mathbf{S} \mathbf{R}, \\ \mathbf{T}^3 = \mathbf{S}^2 - \frac{1}{3} \mathbf{I} \cdot \text{tr}(\mathbf{S}^2), & \mathbf{T}^8 = \mathbf{S} \mathbf{R} \mathbf{S}^2 - \mathbf{S}^2 \mathbf{R} \mathbf{S}, \\ \mathbf{T}^4 = \mathbf{R}^2 - \frac{1}{3} \mathbf{I} \cdot \text{tr}(\mathbf{R}^2), & \mathbf{T}^9 = \mathbf{R}^2 \mathbf{S}^2 + \mathbf{S}^2 \mathbf{R}^2 - \frac{2}{3} \mathbf{I} \cdot \text{tr}(\mathbf{S}^2 \mathbf{R}^2), \\ \mathbf{T}^5 = \mathbf{R} \mathbf{S}^2 - \mathbf{S}^2 \mathbf{R}, & \mathbf{T}^{10} = \mathbf{R} \mathbf{S}^2 \mathbf{R}^2 - \mathbf{R}^2 \mathbf{S}^2 \mathbf{R}, \end{array} \right. \quad (26)$$

$$\begin{aligned} \lambda_1 &= \text{tr}(\mathbf{S}^2), & \lambda_2 &= \text{tr}(\mathbf{R}^2), & \lambda_3 &= \text{tr}(\mathbf{S}^3), & \lambda_4 &= \text{tr}(\mathbf{R}^2 \mathbf{S}), \\ \lambda_5 &= \text{tr}(\mathbf{R}^2 \mathbf{S}^2), & \lambda_6 &= \nabla k \cdot \mathbf{S} \nabla k, & \lambda_7 &= \nabla k \cdot \mathbf{S}^2 \nabla k, & \lambda_8 &= \nabla k \cdot \mathbf{R}^2 \nabla k, \\ \lambda_9 &= \nabla k \cdot \mathbf{S} \mathbf{R} \nabla k, & \lambda_{10} &= \nabla k \cdot \mathbf{S}^2 \mathbf{R} \nabla k, & \lambda_{11} &= \nabla k \cdot \mathbf{R} \mathbf{S} \mathbf{R}^2 \nabla k, & \lambda_{12} &= \nabla k \cdot \nabla k. \end{aligned} \quad (27)$$

It should be noted that the aforementioned invariant set is complete and irreducible, but it is not a minima set. The

training of neural networks may be impacted by the presence of implicit function relationships between invariants, but it has no significant impact in the present study. The research of irreducible complete minima invariants set is planned.

E. Propagation of the predicted anisotropy tensor

The C++ based open source CFD toolbox OpenFOAM is used to simulate the RANS flow field. The $k - \omega$ turbulent model is used in the present study. In the present study, we basically follow this propagation procedure with an underrelaxing coefficient to enhance the conditioning [20]. The Reynold stress $\boldsymbol{\tau}$ is treated as:

$$\boldsymbol{\tau} = \frac{2}{3}k\mathbf{I} + 2k\mathbf{b}_{ML}, \quad (28)$$

where \mathbf{b}_{ML} is obtained from the ML model, and k is calculated by the kinetic energy governing equation with the modified production term $-\boldsymbol{\tau} : \nabla \bar{\mathbf{u}}$.

The procedure of the present study is summarized as follows:

1. Collect the high-fidelity LES/DNS/experimental turbulence data from the turbulence database. Simulate the baseline flow field by OpenFOAM based on $k - \omega$ RANS turbulent model.
2. Calculate the tensor basis \mathbf{T}^n and tensor invariants λ_i based on the RANS results. Calculate the Reynolds stress anisotropy tensor b_{ij} based on high-fidelity turbulent data.
3. Training the regression function $\mathbf{F} : \{\mathbf{T}^n, \lambda_i\} \mapsto \Delta\mathbf{b}$ and $\mathbf{F} : \lambda_i \mapsto \Delta\mathbf{b}$ based on data prepared in the previous step and machine learning algorithm.
4. Propagate the predicted anisotropy tensor into the SIMPLE algorithm with a modified k production term, and the new RANS flow field is simulated.

Fig. 5 represents the training framework of the present study. The flow case data will be divided into a training set and a testing set. The models trained in the present study are the FCNN-5, FCNN-12, TBNN-5 and TBNN-12 models. The FCNN-5 model establishes the regression function of five invariants based on \mathbf{S} and \mathbf{R} with an output of $\Delta\mathbf{b}$. The FCNN-12 is based on the 12 invariants based on \mathbf{S} , \mathbf{R} and ∇k . The output of the FCNN model is $\Delta\mathbf{b} \in \mathbb{R}^{1 \times 6}$. Compared with the FCNN model, the TBNN model will produce the scalar function values $g_i \in \mathbb{R}^{1 \times 10}$ and dot product g_i with tensor basis $\mathbf{T}^n \in \mathbb{R}^{3 \times 3 \times 10}$, and the output tensor is the sum of the products in the third dimension. More specifically, the input layer of FCNN-5 model is five invariants of \mathbf{S} , \mathbf{R} and that of FCNN-12 model is the 12 invariants based on \mathbf{S} , \mathbf{R} and ∇k .

III. RESULTS AND DISCUSSION

A. Turbulence datasets

In the present study, five flow cases are involved in machine learning procedures. The DNS and highly resolved LES data are available. The corresponding RANS data are obtained by the $k - \omega$ turbulent model for the Reynolds stress. Fig. 6 displays the flow cases used in the present study. Five types of relevant flow cases are:

- Periodic hills (PH): The data of periodic hill flow fields are obtained from Breuer et al. [25]. The Reynold number Re ranges from 700 to 10595 ($Re = 700, 1400, 2800, 5600, 10595$). Five cases are included in the present study.
- Converging-diverging channel (CD): The DNS data of the converging-diverging channel flow field is obtained from Marquillie et al. [32] at $Re = 13700$. Public download access to the data is available[33].
- Curved backward-facing step (CBFS): The LES data of curved backward-facing step flow field is obtained from Bentaleb et al.[34] and the Reynold number Re is 12600[35].
- Backward-facing step (BFS): The DNS data of backward-facing step flow field is obtained from Le et al. [36] at $Re = 5100$ [37].
- Square duct (SD): The square duct flow field contains data from eight flow fields with Re ranging from 1800 to 3500 from Pinelli et al. [38]. The Reynolds numbers Re are 1800, 2000, 2200, 2400, 2600, 2900, 3200 and 3500.

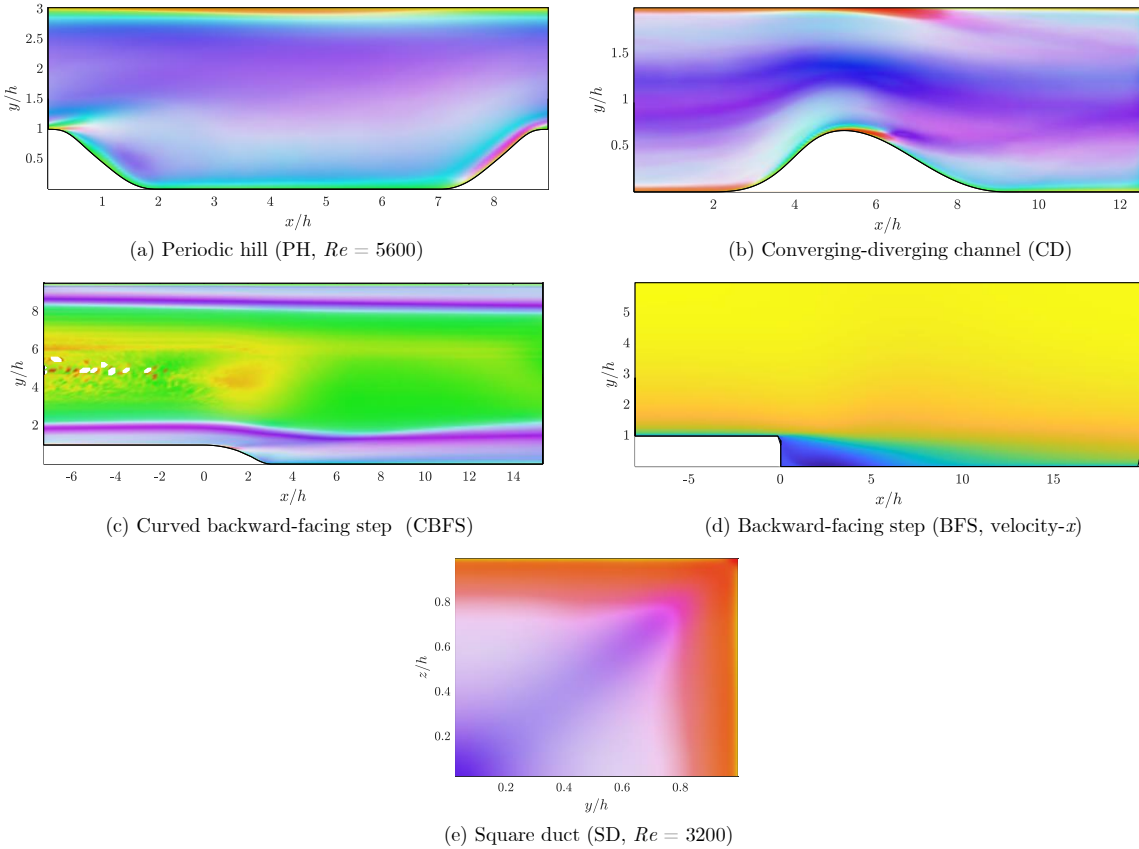


FIG. 6: Flow cases used in the present study. The BFS flow case is displayed through velocity in the x direction (blue represents negative value, yellow represents positive value), and the other flow cases are displayed through the turbulent state. The SD flow case only presents the upper right quadrant of the duct, where the flow in the duct removes-of-plane.

In the present study, the testing set consists of PH ($Re = 5600$) and SD ($Re = 3500$), and the remaining data are the training data of the present study. The MLP model contains 16 hidden layers with a combination of 15, 50, 50,

150, 150, 150, 300, 300, 300, 300, 150, 150, 150, 50, and 15 neurons per layer. Kaiming initialization method [39] is applied to the linear layer. LeakyReLU and batch normalization are used for the activator. The Adam optimizer [40], with a learning rate 1.0×10^{-6} and a decay rate of 0.999, is applied for training. To avoid overfitting, early stopping is applied in the training process.

B. Reynolds stress anisotropy tensor b_{ij} predictions

In this section, the Reynolds stress anisotropy tensors b_{ij} of the test set are displayed. Fig. 7 displays the contour plot of the b_{ij} prediction values of the PH case at $Re = 5600$. The DNS data are obtained from Breuer *et al.* [25]. The b_{ij} of $k - \omega$ turbulent model data is derived from Eq. (6). The input data of the FCNN and TBNN models are normalized by the mean and std values of the training dataset. Since the flow is homogeneous in the z direction, the b_{13} and b_{23} components are zero [41]. Here, we represent the other 4 independent values of b_{ij} .

It can be noticed that the $k - \omega$ turbulent model can only predict the b_{23} component with acceptable accuracy. We can see that the machine learning turbulent model can not only predict the b_{23} values but the rest components. The root mean square error (RMSE) values of different prediction values versus DNS values are displayed in Table II. The machine learning based turbulent models yield much better results than traditional turbulence models based on the Boussinesq hypothesis. While the prediction values of machine learning models show higher accuracy but poor continuity. The machine learning algorithm searches for a mapping relationship between input and output rather than a predetermined function. The results of the machine learning turbulent model in the present study have not been postprocessed, such as with a Gaussian filter. Some data smoothing methods based on prior knowledge are applied to obtain better continuity for machine learning turbulence model prediction. Some researchers choose to obtain the turbulent viscosity coefficient of the Boussinesq hypothesis by machine learning regression [42]. We believe this issue is a research topic deserving further development in this community.

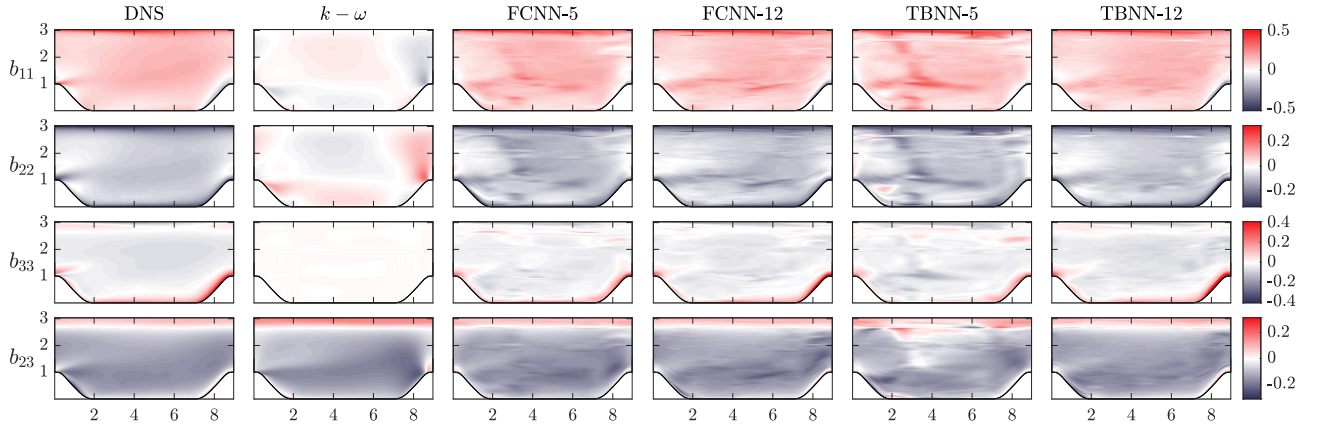


FIG. 7: b_{ij} prediction values of PH at $Re = 5600$. $k - \omega$ data is the RANS turbulent model prediction values.

Both the FCNN and TBNN models can predict more accurate values with more inputs, as shown in Table I. The involvement ∇k will increase the predictions of b_{ij} . b_{ij} prediction values by the FCCN model are more accurate compared with the TBNN model. In the FCCN model, a direct mapping between the invariants of fluid data and the Reynold stress anisotropy tensor is established. The FCNN model adds a restriction of the scalar function g_i with a

certain function structure, which decreases the overall neural network's capacity, similar to the PINN model [6].

TABLE I: RMSE values of b_{ij} predictions of different models on the periodic hill case.

Model	RANS	FCNN-5	FCNN-12	TBNN-5	TBNN-12
RMSE	0.0984	0.0357	0.0324	0.0469	0.0307

Fig. 8 represents the turbulent states of different turbulent models in PH flow at $Re = 5600$. The contours are colored by the RGB colormap shown in Fig. 1. It can be seen that there exists 1-component turbulence (red) along the upper wall and 2-component turbulence (green) close to the upper and lower walls. At $x/h = 8$, there exists a strong 1-component turbulence, which is named the splatting effect [43].

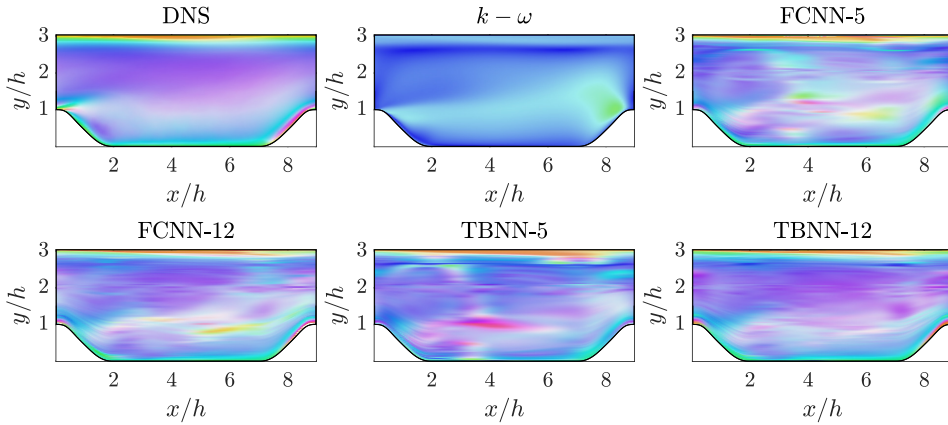


FIG. 8: Turbulent states of different turbulent models in PH flow case visualized with the RGB colormap in Fig. 1.

The $k - \omega$ turbulent model cannot predict any turbulent state precisely, and it remains a plane strain turbulent state. In the splatting effect region, the large-scale eddies generated in the shear layer are convected downstream onto the upward slope, causing a high level of fluctuations in the z-direction. This also indicates that eddy viscosity models, which do not take into account such transport effects, will not be able to capture high anisotropy due to splatting. Thus, the machine learning-based turbulent model can predict these near-wall turbulent states with better precision than the $k - \omega$ model. There also exists the continuity drawback for the machine learning based turbulent model, but the TBNN model is smoother than the FCNN model, due to the FCNN-12 and TBNN-12 model execute predictions with form constraints.

Fig. 9 represents the b_{ij} prediction values of the square duct flow case at $Re = 5600$. All six components of b_{ij} are nonzero. The $k - \omega$ turbulent model predicts zero values in b_{11} , b_{22} , b_{33} and b_{23} since the RANS simulation does not yield any velocities in the y direction and z direction, and the velocity in the x direction is fully developed with $\frac{\partial \bar{u}}{\partial x} = 0$.

Table II displays the RMSE values of b_{ij} prediction values of different models compared with DNS data. Similar to the periodic hill flow case, the model with ∇k will produce a better prediction of b_{ij} .

Fig. 10 represents the turbulent states of different turbulent models in the SD flow case at $Re = 3500$. It can be seen that in most regions, the turbulent state presents a mix of 1-component turbulence and 3-component turbulence. The velocity fluctuation in the x direction u dominates the turbulence of the 1-component turbulent state. Within

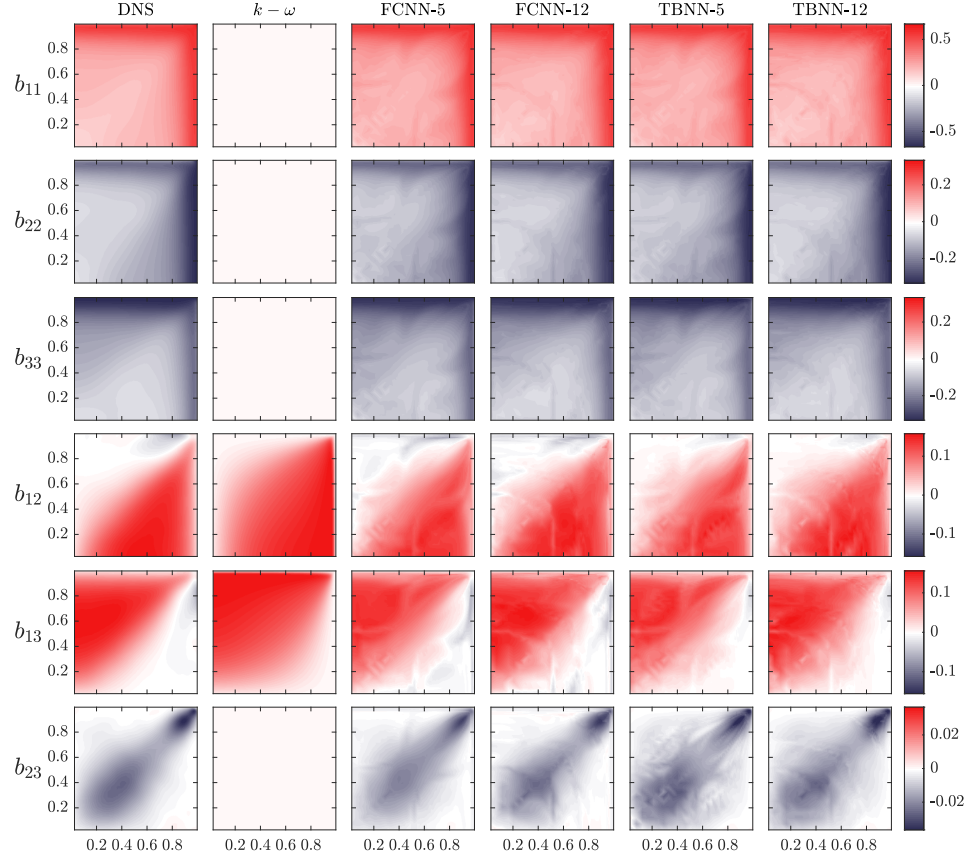


FIG. 9: b_{ij} prediction values of SD at $Re = 5600$. $k - \omega$ data are the RANS turbulent model prediction values.

TABLE II: RMSE values of b_{ij} predictions of different models on the square duct case.

Model	RANS	FCNN-5	FCNN-12	TBNN-5	TBNN-12
RMSE	0.1972	0.0139	0.0098	0.0174	0.0142

the diagonal region of the flow case, the 3-component turbulent state is dominant with interaction with velocity in the y and z directions. The machine learning-based turbulent model can predict the 1-component turbulent well of the near wall. The machine learning turbulent model prediction values lack continuity when modeling a mixed turbulent state. However, the $k - \omega$ turbulent model cannot produce a precise turbulent state.

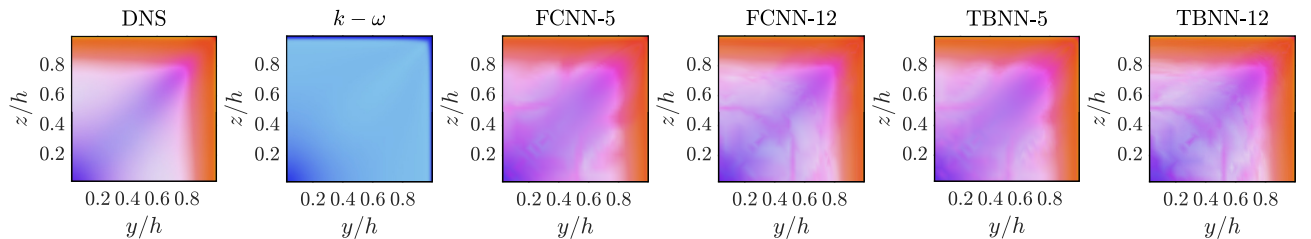


FIG. 10: Turbulent states of different turbulent models in the SD flow case visualized with the RGB colormap in Fig. 1.

C. Flow velocity profile predictions

The flow fields obtained by propagating the Reynold stress anisotropy tensor (as stated above) are displayed. The flow velocity profile based on $b_{ij,DNS}$ is obtained by propagating the Reynolds stress anisotropy tensor from high-fidelity data. It's the best performance ML based turbulent model capable of in flow velocity profile prediction. Fig. 11 represents the flow velocity distribution in the periodic hill flow case at $Re = 5600$. The velocity distribution of the RANS model is close to that of the DNS result even with inaccurate turbulent state prediction. The velocity profile with machine learning-based b_{ij} only slightly increases the accuracy in the flow field prediction.

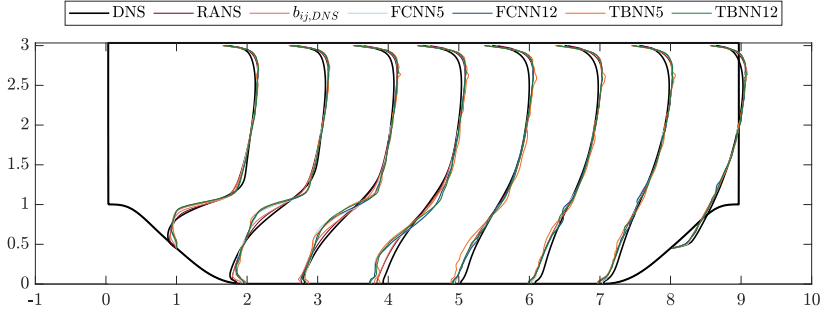


FIG. 11: Predicted flow velocity distribution in the periodic hill flow case. The RANS values are obtained from the $k - \omega$ model. The $b_{ij,DNS}$ data are obtained by propagating the b_{ij} of the DNS data.

Fig. 12 represents the in-plane mean velocity magnitude $\sqrt{u_y^2 + u_z^2}$ (u_y represents the velocity component in the y direction, coordinate of square duct flow case is shown in Fig. 6), which indicates the magnitude of the secondary flow of the square duct. It has proven difficult to predict square duct secondary flow using conventional turbulence models. Here one section $y/h = 0.50$ in the square duct flow case at $Re = 3500$ is represented. The DNS data, and the data obtained from DNS b_{ij} and predicted b_{ij} are shown. Furthermore, the results from the quadratic eddy viscosity model [44] and cubic eddy viscosity model [45] are displayed. The RANS data based on $k - \omega$ turbulent model are omitted here since the magnitude remains zero. Compared with periodic hill flow case, Reynolds stress anisotropy has a bigger impact on the square cavity flow. The anisotropic Reynolds stress is a significant factor for secondary flow [38]. The machine learning based turbulent model can predict the component of b_{ij} in the flow direction (x direction) which results in a better velocity profile prediction.

The DNS mean velocity profile is roughly reproduced by propagating $b_{ij,DNS}$. The peak value and location are predicted well. The near-wall region ($z/h \approx 1$) matches well with the DNS data, and the location of the peak value in region $z/h \in [0.3, 0.8]$ is incorrectly predicted with an error of 0.10. The worst prediction occurs near $z/h = 0$. The TBNN-12 model achieves relatively exact prediction, with reduced amplitude in the machine learning-based turbulent model predictions. While FCNN can produce b_{ij} predictions with reduced RMSE, the TBNN model achieved a slightly accurate prediction in the region $z/h \in [0.3, 0.8]$. Therefore, the form constraint with prior physical or mathematics knowledge can improve the prediction of flow velocity profiles. For the nonlinear eddy viscosity turbulent model, the prediction peak values of the in-plane velocity magnitude are quite poor. The quadratic turbulent model in Shih [44] can produce relatively correct flow velocity trends but with insufficient amplitude. Meanwhile, the prediction values given by the cubic turbulent model in Lien [45] are generally incorrect. Compared with the nonlinear eddy viscosity model, the machine learning-based turbulent model predicts a much more accurate velocity profile. Nevertheless, the

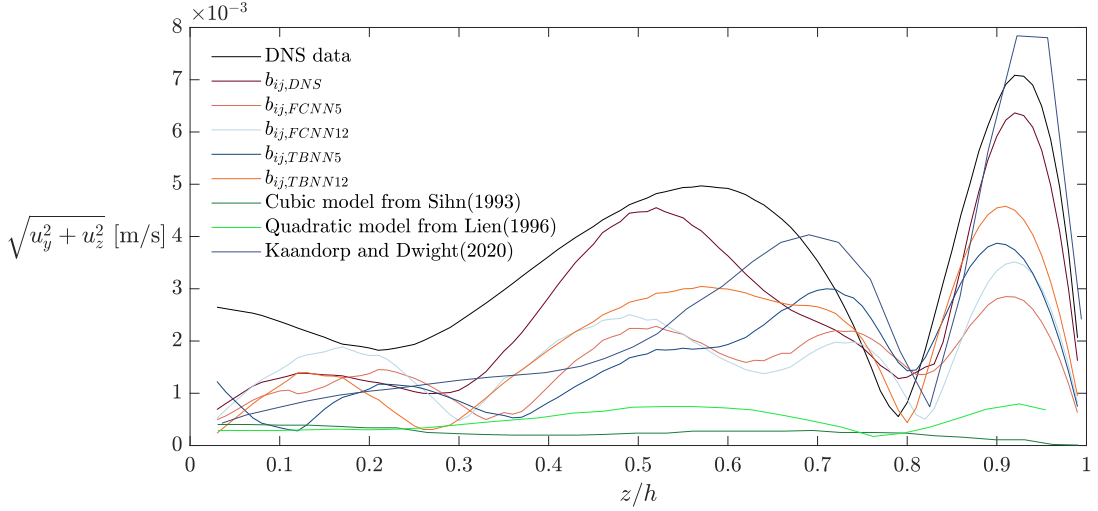


FIG. 12: In-plane mean velocity profiles at section $y/h = 0.50$ of the square duct at $Re = 3500$. The cubic and quadratic models are nonlinear eddy viscosity models in Shih [44] and Lien [45]. Kaandorp and Dwight [41] is the velocity profile prediction based on random forest algorithm.

b_{ij} profile is highly sensitive to the velocity profile, and even a small change in b_{ij} can result in a different velocity profile, such as is seen in the TBNN-12 and FCNN-12 models. Kaandorp and Dwight [41] displays the velocity profile prediction based on random forest algorithm with five invariants same with FCNN-5. This bagging based algorithm is different from the FCNN, gradient decent based algorithm, applied in the present study. It can be seen that it overrated the mean velocity in the range $y/h > 0.80$, and the prediction is close to five invariants based algorithm in the range $y/h < 0.80$. They incorporate several additional features (like Reynolds number) into the model training process, which may increase the accuracy to specific flow fields predictions. The ultimate goal of machine learning based turbulent model is to implement turbulence simulation with high generalization capability, and appropriate feature selection is continuously being researched. Future studies should aim to enhance the continuity of the turbulence model based on machine learning. Schmelzer *et al.* [46] and Weatheritt and Sandberg [47] proposed different symbolic regression methods to develop an explicit formula to enhance the continuity and numerical stability. However, these methods have only been applied to establish mapping $\mathbf{S}, \mathbf{R} \mapsto \mathbf{b}$. A more accurate turbulent model based on more invariants will be investigated in the future.

IV. CONCLUSION

In the present study, a comparative study of Reynolds stress tensor prediction methods based on invariance preservation is studied. Two kinds of machine learning structures, FCNN and TBNN, are investigated. Two invariant input sets based on \mathbf{S}, \mathbf{R} and $\mathbf{S}, \mathbf{R}, \nabla k$ are considered. The models are trained based on RANS flow fields ($k - \omega$) for input and the anisotropy tensor from high-fidelity data for output. Tensor basis neural network [20] and fully connected neural network are applied for training. Machine learning based on invariants ensures Galilean invariance of the turbulent model.

The prediction of the Reynold stress anisotropy tensor b_{ij} and flow profile by propagating b_{ij} are investigated in the

present study. Improvement is observed with respect to the baseline simulations with the $k - \omega$ model. The FCNN model obtains a better prediction of b_{ij} but shows less accuracy in the flow velocity profile compared with TBNN model. The TBNN model involves a form of constraint based on prior knowledge and improves the turbulent states. The inclusion of ∇k can increase the prediction accuracy of the Reynold stress anisotropy tensor and flow velocity profile in comparison to the invariants defined based on \mathbf{S} , \mathbf{R} . Compared with the traditional nonlinear turbulent model [44, 45], the machine learning-based turbulent model can improve the Reynolds stress anisotropy tensor and flow velocity profile prediction.

The drawback of the present study is that the continuity of b_{ij} are relatively poor. Research on the explicit symbolic regression method [46, 47] can be further applied for the invariant set \mathbf{S} , \mathbf{R} , ∇k , ...-based turbulent model, different from the implicit gradient decent-based MLP model as used here. Such a modification may improve the numerical stability and accuracy of the present work.

DATA AVAILABILITY

The code for the neural network training will be made available in a public Github repository: github.com/Fussa42/tbnn_pytorch. The code is developed based on Pytorch.

ACKNOWLEDGMENTS

The authors gratefully acknowledge the financial support from the National Natural Science Foundation of China under Grant Number of 52088102, the Joint Funds of the National Natural Science Foundation of China under Grant Number of U19B2013, National Natural Science Foundation of China under Grant Number of 52001208, 51909159, 52111530135, Shanghai Science and Technology Program under Grant Number of 21ZR1434500, 19XD1402000 and 19JC1412801, National Science Fund for Distinguished Young Scholars under Grant Number of 51825903, State Key Laboratory of Ocean Engineering (Shanghai Jiao Tong University) under Grant Number of GKZD010081, Shenlan Project under Grant Number of SL2020PT102 and SL2021MS018, Young Elite Scientists Sponsorship Program under Grant Number of 2020QNRC001. In addition, the authors would like to express their gratitude to Dr.Mikael Kaandorp, who shared the highly resolved flow field data collected previously.

Appendix A: Scalar invariants of symmetric and antisymmetric tensors

For any second order tensor $P_{ij} \in \mathbb{R}^{3 \times 3}$, we can deliver a symmetric tensor S_{ij} and antisymmetric tensor W_{ij} as:

$$S_{ij} = \frac{1}{2}(P_{ij} + P_{ji}), \quad (\text{A1})$$

$$W_{ij} = \frac{1}{2}(P_{ij} - P_{ji}). \quad (\text{A2})$$

For a symmetric tensor, a simpler form based on the principal axis system can be expressed as:

$$S_{ij} = \begin{bmatrix} e_1 & 0 & 0 \\ 0 & e_2 & 0 \\ 0 & 0 & e_3 \end{bmatrix}, \quad (\text{A3})$$

where e_i is the principal components of S_{ij} in the direction of the principal axis. And the antisymmetric tensor can be expressed as:

$$W_{ij} = \frac{1}{2} \begin{bmatrix} 0 & \omega_3 & \omega_2 \\ -\omega_3 & 0 & \omega_1 \\ -\omega_2 & -\omega_1 & 0 \end{bmatrix}. \quad (\text{A4})$$

There are three main invariants of S_{ij} expressed as:

$$\begin{aligned} J_1 &= e_1 + e_2 + e_3, \\ J_2 &= e_1^2 + e_2^2 + e_3^2, \\ J_3 &= e_1^3 + e_2^3 + e_3^3. \end{aligned} \quad (\text{A5})$$

Additionally, widely used invariants called principle invariants are expressed as follows:

$$\begin{aligned} I_1 &= \text{tr}(S_{ij}) = e_1 + e_2 + e_3, \\ I_2 &= \frac{1}{2} ((\text{tr}(S_{ij}))^2 - \text{tr}(S_{ij}^2)) = e_1 e_2 + e_1 e_3 + e_2 e_3, \\ I_3 &= \det(S_{ij}) = e_1 e_2 e_3. \end{aligned} \quad (\text{A6})$$

The relationship between I_i and J_i is:

$$\begin{aligned} J_1 &= I_1, \\ J_2 &= I_1^2 - 2I_2, \\ J_3 &= I_1^3 - 3I_1 I_2 + 3I_3. \end{aligned} \quad (\text{A7})$$

In [30, 31, 48], they all state that there exist seven invariants based on symmetric and antisymmetric tensors:

$$\begin{aligned} \lambda_1 &= \text{tr}(S_{ij}), \quad \lambda_2 = \text{tr}(S_{ij}^2), \quad \lambda_3 = \text{tr}(S_{ij}^3), \\ \lambda_4 &= \text{tr}(W_{ij}^2), \quad \lambda_5 = \text{tr}(S_{ij} W_{ij}^2), \quad \lambda_6 = \text{tr}(S_{ij}^2 W_{ij}^2), \quad \lambda_7 = \text{tr}(S_{ij}^2 W_{ij}^2 S_{ij} W_{ij}). \end{aligned} \quad (\text{A8})$$

However, Pope [18] only used the first six invariants for turbulent modeling. Pope and the reference [27] have not clarified it, which induced some reference mistakes [49]. In the following, we will prove that λ_7 can be expressed as a function of the first six invariants.

Following the above representation of S_{ij} and W_{ij} , we can have the invariants $\lambda_1 = J_1$, $\lambda_2 = J_2$ and $\lambda_3 = J_3$. λ_4 can be expressed as:

$$\lambda_4 = \text{tr}(W_{ij}^2) = -\frac{1}{2}(w_1^2 + w_2^2 + w_3^2), \quad (\text{A9})$$

and λ_5 is:

$$\lambda_5 = \text{tr}(S_{ij} W_{ij}^2) = -\frac{1}{4}(e_1 w_2^2 + e_2 w_1^2 + e_1 w_3^2 + e_3 w_1^2 + e_2 w_3^2 + e_3 w_2^2). \quad (\text{A10})$$

We assume that $J_1 = 0$ for representation simplification (this conclusion also holds when $J_1 \neq 0$), which can deliver:

$$\lambda_5 = \frac{1}{4}(e_1 w_1^2 + e_2 w_2^2 + e_3 w_3^2). \quad (\text{A11})$$

The λ_6 can be expressed as:

$$\lambda_6 = \text{tr}(S_{ij}^2 W_{ij}^2) = -\frac{1}{4}(e_1^2 w_2^2 + e_2^2 w_1^2 + e_1^2 w_3^2 + e_3^2 w_1^2 + e_2^2 w_3^2 + e_3^2 w_2^2). \quad (\text{A12})$$

Considering the main invariants, the λ_6 can be simplified as:

$$\lambda_6 = -\frac{1}{4} [(2J_2 - J_1)(w_1^2 + w_2^2 + w_3^2) - (e_1^2 w_1^2 + e_2^2 w_2^2 + e_3^2 w_3^2)], \quad (\text{A13})$$

and the last invariants λ_7 can be expressed as:

$$\lambda_7 = \text{tr}(S_{ij}^2 W_{ij}^2 S_{ij} W_{ij}) = \frac{1}{8} w_1 w_2 w_3 (e_1^2 e_2 - e_1^2 e_3 - e_1 e_2^2 + e_1 e_3^2 + e_2^2 e_3 - e_2 e_3^2) \quad (\text{A14})$$

$$= \frac{1}{8} (e_2 - e_1)(e_3 - e_2)(e_1 - e_3) w_1 w_2 w_3. \quad (\text{A15})$$

We can see that λ_7 is the function based on w_i . It is easy to find three invariants based on w_i^2 from λ_4 , λ_5 and λ_6 :

$$K_1 = w_1^2 + w_2^2 + w_3^2, \quad (\text{A16})$$

$$K_2 = e_1 w_1^2 + e_2 w_2^2 + e_3 w_3^2, \quad (\text{A17})$$

$$K_3 = e_1^2 w_1^2 + e_2^2 w_2^2 + e_3^2 w_3^2. \quad (\text{A18})$$

This equation can be solved as follows:

$$w_1^2 = \frac{(K_3 - K_2 e_2 - K_2 e_3 + K_1 e_2 e_3)}{(e_1 - e_2)(e_1 - e_3)}, \quad (\text{A19})$$

$$w_2^2 = \frac{(K_3 - K_2 e_1 - K_2 e_3 + K_1 e_1 e_3)}{(e_2 - e_1)(e_2 - e_3)}, \quad (\text{A20})$$

$$w_3^2 = \frac{(K_3 - K_2 e_1 - K_2 e_2 + K_1 e_1 e_2)}{(e_1 - e_3)(e_2 - e_3)}. \quad (\text{A21})$$

Considering $J_1 = 0$, w_i can be solved as:

$$w_1^2 = \frac{(K_3 + K_2 e_1 + K_1 e_2 e_3)}{(e_1 - e_2)(e_1 - e_3)}, \quad (\text{A22})$$

$$w_2^2 = \frac{(K_3 + K_2 e_2 + K_1 e_1 e_3)}{(e_2 - e_1)(e_2 - e_3)}, \quad (\text{A23})$$

$$w_3^2 = \frac{(K_3 + K_2 e_3 + K_1 e_1 e_2)}{(e_1 - e_3)(e_2 - e_3)}. \quad (\text{A24})$$

Thus, λ_7^2 can be expressed as:

$$\lambda_7^2 = [\text{tr}(S_{ij}^2 W_{ij}^2 S_{ij} W_{ij})]^2 = \frac{1}{64} (e_2 - e_1)^2 (e_3 - e_2)^2 (e_1 - e_3)^2 w_1^2 w_2^2 w_3^2 \quad (\text{A25})$$

$$= \frac{1}{128} [2K_1^3 I_3 + 2K_1 K_2 I_3 J_3 + 2K_1^2 K_3 I_3 J_1 \quad (\text{A26})$$

$$+ K_1 K_2^2 (J_2^2 - J_1 J_3 - I_3 J_2 + J_2 I_2) \quad (\text{A27})$$

$$+ 2K_1 K_2 K_3 (J_1 J_2 - J_3) + 2K_1 K_3^2 I_2 + K_3^2 I_3 \quad (\text{A28})$$

$$+ 2K_2^2 K_3 I_2 + 2K_2 K_3^2 I_1 + 2K_3^3], \quad (\text{A29})$$

which means $\lambda_7^2 = f(\lambda_1, \lambda_2, \lambda_3, \lambda_4, \lambda_5, \lambda_6)$, so the seven invariants are not independent. There only exist six independent invariants of λ_1 to λ_6 . In fact, this phenomenon is called syzygy in tensor function community, which means that the invariants are related by an implicit function. In [30, 31, 48], the complete set of invariants is given, not a minimum complete set. In the training process based on tensor function theory, there may exist inappropriate data weights of different invariants.

Appendix B: Basis tensor and scalar function

We reshape the output anisotropy tensor $\mathbf{b}_{3 \times 3}$ and input tensor basis $\mathbf{B}_{3 \times 3 \times 10}$ as $\mathbf{b}_{9 \times 1}$ and $\mathbf{B}_{9 \times 10}$, respectively. Then we have:

$$\mathbf{B}_{9 \times 10} \cdot \mathbf{C}_{10 \times 1} = \mathbf{b}_{9 \times 1}, \quad (\text{B1})$$

where $\mathbf{C}_{10 \times 1}$ is the scalar function value g_i in Eq. (20). $\mathbf{C}_{10 \times 1}$ can be estimated by the least squares method as:

$$\mathbf{C}_{10 \times 1} = (\mathbf{B}_{9 \times 10}^T \mathbf{B}_{9 \times 10})^{-1} \mathbf{B}_{9 \times 10}^T \mathbf{b}_{9 \times 1}. \quad (\text{B2})$$

Fig. 13 displays the absolute scalar function values $|g_8|$ based on b_{ij} and Δb_{ij} in the BFS case. It can be seen that the scalar function values can be slightly reduced based on Δb_{ij} compared with b_{ij} . Fig. 14 displays the contour plot of the tensor basis $T^{(1)}$ of the square duct flow case at $Re = 3500$.

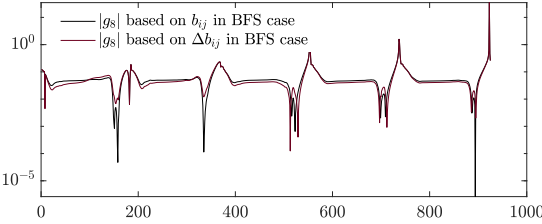


FIG. 13: Absolute scalar function values $|g_8|$ based on b_{ij} and Δb_{ij} in the backward-facing step flow case. $|g_8|$ is the eighth value of $\mathbf{C}_{10 \times 1}$ obtained based on Eq. (B2).

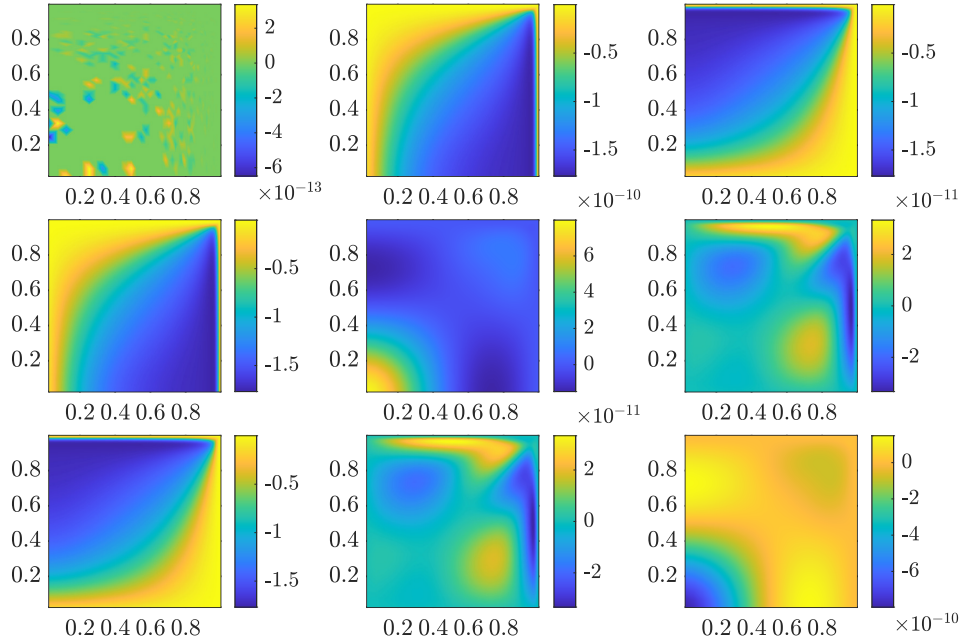


FIG. 14: Visualization of tensor basis $T^{(1)}$ in the SD flow case at $Re = 3500$. $T^{(1)}$ is second order tensor with six independent value, the subplots correspond to the contours of each component.

-
- [1] J. P. Slotnick, A. Khodadoust, J. Alonso, D. Darmofal, W. Gropp, E. Lurie, and D. J. Mavriplis, *CFD vision 2030 study: a path to revolutionary computational aerosciences*, Tech. Rep. (2014).
- [2] D. C. Wilcox *et al.*, *Turbulence modeling for CFD*, Vol. 2 (DCW industries La Canada, CA, 1998).
- [3] T. Craft, B. Launder, and K. Suga, Development and application of a cubic eddy-viscosity model of turbulence, *International Journal of Heat and Fluid Flow* **17**, 108 (1996).
- [4] K. Duraisamy, G. Iaccarino, and H. Xiao, Turbulence modeling in the age of data, *Annual Review of Fluid Mechanics* **51**, 357 (2019).
- [5] M. Milano and P. Koumoutsakos, Neural network modeling for near wall turbulent flow, *Journal of Computational Physics* **182**, 1 (2002).
- [6] M. Raissi, P. Perdikaris, and G. E. Karniadakis, Physics-informed neural networks: A deep learning framework for solving forward and inverse problems involving nonlinear partial differential equations, *Journal of Computational physics* **378**, 686 (2019).
- [7] R. Xu, X.-H. Zhou, J. Han, R. P. Dwight, and H. Xiao, A pde-free, neural network-based eddy viscosity model coupled with rans equations, *International Journal of Heat and Fluid Flow* **98**, 109051 (2022).
- [8] B. Tracey, K. Duraisamy, and J. Alonso, Application of supervised learning to quantify uncertainties in turbulence and combustion modeling, in *51st AIAA aerospace sciences meeting including the new horizons forum and aerospace exposition* (2013) p. 259.
- [9] K. Duraisamy, Z. J. Zhang, and A. P. Singh, New approaches in turbulence and transition modeling using data-driven techniques, in *53rd AIAA Aerospace sciences meeting* (2015) p. 1284.
- [10] Z. J. Zhang and K. Duraisamy, Machine learning methods for data-driven turbulence modeling, in *22nd AIAA computational fluid dynamics conference* (2015) p. 2460.
- [11] J. Ling and J. Templeton, Evaluation of machine learning algorithms for prediction of regions of high reynolds averaged navier-stokes uncertainty, *Physics of Fluids* **27**, 085103 (2015).
- [12] X.-L. Zhang, H. Xiao, X. Luo, and G. He, Ensemble kalman method for learning turbulence models from indirect observation data, *Journal of Fluid Mechanics* **949**, A26 (2022).
- [13] M. Emory, J. Larsson, and G. Iaccarino, Modeling of structural uncertainties in reynolds-averaged navier-stokes closures, *Physics of Fluids* **25**, 110822 (2013).
- [14] H. Xiao, J.-L. Wu, J.-X. Wang, R. Sun, and C. Roy, Quantifying and reducing model-form uncertainties in reynolds-averaged navier-stokes simulations: A data-driven, physics-informed bayesian approach, *Journal of Computational Physics* **324**, 115 (2016).
- [15] H. Xiao and P. Cinnella, Quantification of model uncertainty in rans simulations: A review, *Progress in Aerospace Sciences* **108**, 1 (2019).
- [16] J.-L. Wu, R. Sun, S. Laizet, and H. Xiao, Representation of stress tensor perturbations with application in machine-learning-assisted turbulence modeling, *Computer Methods in Applied Mechanics and Engineering* **346**, 707 (2019).
- [17] J. Ling, R. Jones, and J. Templeton, Machine learning strategies for systems with invariance properties, *Journal of Computational Physics* **318**, 22 (2016).
- [18] S. Pope, A more general effective-viscosity hypothesis, *Journal of Fluid Mechanics* **72**, 331 (1975).
- [19] A. J. M. Spencer and R. S. Rivlin, Isotropic integrity bases for vectors and second-order tensors, in *Collected Papers of R.S. Rivlin: Volume I and II*, edited by G. I. Barenblatt and D. D. Joseph (Springer New York, New York, NY, 1997) pp. 1243–1261.

- [20] J. Ling, A. Kurzawski, and J. Templeton, Reynolds averaged turbulence modelling using deep neural networks with embedded invariance, *Journal of Fluid Mechanics* **807**, 155 (2016).
- [21] F. R. Menter, Two-equation eddy-viscosity turbulence models for engineering applications, *AIAA journal* **32**, 1598 (1994).
- [22] B. E. Launder, G. J. Reece, and W. Rodi, Progress in the development of a reynolds-stress turbulence closure, *Journal of fluid Mechanics* **68**, 537 (1975).
- [23] S. Banerjee, R. Krahl, F. Durst, and C. Zenger, Presentation of anisotropy properties of turbulence, invariants versus eigenvalue approaches, *Journal of Turbulence* , N32 (2007).
- [24] J. L. Lumley and G. R. Newman, The return to isotropy of homogeneous turbulence, *Journal of Fluid Mechanics* **82**, 161 (1977).
- [25] M. Breuer, N. Peller, C. Rapp, and M. Manhart, Flow over periodic hills—numerical and experimental study in a wide range of reynolds numbers, *Computers & Fluids* **38**, 433 (2009).
- [26] J. L. Lumley, Computational modeling of turbulent flows, *Advances in Applied Mechanics* **18**, 123 (1979).
- [27] A. J. M. Spencer and R. S. Rivlin, The theory of matrix polynomials and its application to the mechanics of isotropic continua, *Archive for Rational Mechanics and Analysis* **2**, 309 (1958).
- [28] C.-C. Wang, A new representation theorem for isotropic functions: An answer to professor gf smith's criticism of my papers on representations for isotropic functions, *Archive for Rational Mechanics and Analysis* **36**, 166 (1970).
- [29] G. Smith, On isotropic functions of symmetric tensors, skew-symmetric tensors and vectors, *International Journal of Engineering Science* **9**, 899 (1971).
- [30] A. C. Eringen, *Mechanics of continua*, Huntington (1980).
- [31] Q.-S. Zheng, Theory of representations for tensor functions—a unified invariant approach to constitutive equations, *Applied Mechanics Reviews* (1994).
- [32] M. Marquillie, U. Ehrenstein, and J.-P. Laval, Instability of streaks in wall turbulence with adverse pressure gradient, *Journal of Fluid Mechanics* **681**, 205 (2011).
- [33] https://turbmodels.larc.nasa.gov/Other_DNS_Data/conv-div-channel12600.html.
- [34] Y. Bentaleb, S. Lardeau, and M. A. Leschziner, Large-eddy simulation of turbulent boundary layer separation from a rounded step, *Journal of Turbulence* , N4 (2012).
- [35] https://turbmodels.larc.nasa.gov/Other_LES_Data/curvedstep.html.
- [36] H. Le, P. Moin, and J. Kim, Direct numerical simulation of turbulent flow over a backward-facing step, *Journal of Fluid Mechanics* **330**, 349 (1997).
- [37] [http://cfd.mace.manchester.ac.uk/ercoftac/doku.php?id=cases:case031&s\[\]=backward&s\[\]=facing&s\[\]=step](http://cfd.mace.manchester.ac.uk/ercoftac/doku.php?id=cases:case031&s[]=backward&s[]=facing&s[]=step).
- [38] A. Pinelli, M. Uhlmann, A. Sekimoto, and G. Kawahara, Reynolds number dependence of mean flow structure in square duct turbulence, *Journal of fluid Mechanics* **644**, 107 (2010).
- [39] K. He, X. Zhang, S. Ren, and J. Sun, Delving deep into rectifiers: Surpassing human-level performance on imagenet classification, in *Proceedings of the IEEE international conference on computer vision* (2015) pp. 1026–1034.
- [40] D. P. Kingma and J. Ba, Adam: A method for stochastic optimization, arXiv preprint arXiv:1412.6980 (2014).
- [41] M. L. Kaandorp and R. P. Dwight, Data-driven modelling of the reynolds stress tensor using random forests with invariance, *Computers & Fluids* **202**, 104497 (2020).
- [42] J. Wu, H. Xiao, R. Sun, and Q. Wang, Reynolds-averaged navier–stokes equations with explicit data-driven reynolds stress closure can be ill-conditioned, *Journal of Fluid Mechanics* **869**, 553–586 (2019).
- [43] J. Fröhlich, C. P. Mellen, W. Rodi, L. Temmerman, and M. A. Leschziner, Highly resolved large-eddy simulation of separated flow in a channel with streamwise periodic constrictions, *Journal of Fluid Mechanics* **526**, 19 (2005).
- [44] T.-H. Shih, *A realizable Reynolds stress algebraic equation model*, Vol. 105993 (National Aeronautics and Space Administration, 1993).

- [45] F.-S. Lien, Low-reynolds-number eddy-viscosity modelling based on non-linear stress-strain/vorticity relations, in *Proc. 3rd Symposium On Engineering Turbulence Modelling and Measurements* (1996) pp. 1–10.
- [46] M. Schmelzer, R. P. Dwight, and P. Cinnella, Discovery of algebraic reynolds-stress models using sparse symbolic regression, *Flow, Turbulence and Combustion* **104**, 579 (2020).
- [47] J. Weatheritt and R. Sandberg, A novel evolutionary algorithm applied to algebraic modifications of the rans stress–strain relationship, *Journal of Computational Physics* **325**, 22 (2016).
- [48] R. W. Johnson, *Handbook of fluid dynamics* (Crc Press, 2016).
- [49] S. Berrone and D. Oberto, An invariances-preserving vector basis neural network for the closure of reynolds-averaged navier–stokes equations by the divergence of the reynolds stress tensor, *Physics of Fluids* **34**, 095136 (2022).